# The Effect of Casting Flow Defects on the Flexural Behavior of 2-way UHPFRC Slabs Investigated by Digital Image Correlation and Magnetic Assessment

**Author(s) & Affiliation:**

Marc-Antoine Baril [(1)], Luca Sorelli [(1)], Julien Réthoré [(2)]; Florent Baby [(3)], François Toutlemonde [(3)], Liberato Ferrara [(4)] , Marco Faifer [(4)] and Sébastien Bernardi [(5)]

(1) CRIB, Université Laval, 2325 rue de l'université, Québec, QC, G1V 0A6, Canada
(2) LaMCos INSA Lyon, 18-20, rue des Sciences, F69621  Villeurbanne cedex, France
(3) UPE-IFSTTAR, 14-20 boulevard Newton, 77447 Marne-la-Vallée Cedex 2, France
(4) Politecnico di Milano, Piazza Leonardo da Vinci, 32 20133 Milano, Italy.
(5) Ductal, LafargeHolcim - 61 rue des Belles Feuilles, BP 40, 75782 Paris cedex 16 – France

**Abstract:**

Structural applications of Ultra High Performance Fiber Reinforced Concrete (UHPFRC) have been emerging worldwide thanks to the outstanding tensile strength and ductility of this category of materials. From a design point of view, a critical aspect is to guarantee the ductility of the structural response associated to local material non-brittleness, which strongly depends on the fiber dispersion and orientation. This work aims at considering the effect of fiber orientation on the biaxial behavior of UHPFRC slabs for composite bridges. Several square slabs made of UHPFRC were cast by changing the concrete flow direction and the position of internal cold joints. The slabs were tested under biaxial bending under hyperstatic conditions. The fiber orientation was measured by a non-destructive method based on the magnetic properties of the composite, while the damage process, with emphasis on the microcrack formation and the crack opening, was measured by 3D digital image correlation. Finally, approaches based on the yield line method were employed to analyze the experimental results with respect to the measured fiber orientation and crack distribution. The results of the present work show the important effect of fiber orientation on the ductility of UHPFRC slabs and the ability of combining magnetic methods and Digital Image Correlation (DIC) analyses to capture those effects.

**Keywords:**

Ultra high performance fiber reinforced concrete, slab, fiber orientation, non-destructive magnetic method, digital image correlation, thin slabs, flow casting defect.

## 1.  Introduction

Ultra High Performance Fiber Reinforced Concretes (UHPFRC) have been emerging worldwide in several structural applications thanks to their outstanding tensile strength and ductility (Russell and Graybeal, 2013; Schmidt and Fehling, 2005; Toutlemonde and Resplendino, 2011). A critical aspect is to guarantee the ductility of the structural response associated to the effect of fiber orientation (Resplendino, 2004). UHPFRC have been widely applied to thin structures for which the wall effects favor a rather bi-dimensional and beneficial

fiber orientation (Ferrara et al., 2012), such as, bridge decks (Toulemonde and Resplendino, 2013; Toutlemonde et al., 2005), shell elements (Aubry et al., 2015; Ter Maten et al., 2013); topping layers (Marchand et al., 2012b) and rehabilitation (Brühwiler and Denarie, 2008).

Recently, Moreillon et al. have experimentally studied the structural response of two-ways thin slabs made of UHPFRC varying the effect of fiber volume content (from 0% to 2%), the ratio of passive steel reinforcement (from 0-2.6%) and slab thickness (15-60 mm; 0.59-2.36 in) (Moreillon et al., 2012). The unreinforced UHPFRC slabs underwent flexural failure with rather intricate cross shaped cracks and distributed radial micro-cracks as visualized at the end of test. Moreover, approaches based on the yield limit analysis have been employed to predict fairly well the maximum load of thin UHPFRC slabs with flexural collapse mode, albeit showing the importance of considering the deformation due to microcracks in the estimation of the ultimate deformation (Marchand et al., 2012a).

This work aims at further investigating the effect of fiber orientation on 2-way thin slabs made of UHPFRC with a prearranged discontinuity of the casting flow detected by means of Digital Image Correlation (DIC) and the Magnetic-Inductance Method (MIM). While DIC allows detecting the microcracks process, the MIM allows measuring the fiber dispersion and orientation.

## 2. Materials and Methods

### 2.1. UHPFRC material and slab sample preparation

A commercial UHPFRC (Ductal FM™) was employed, with a volume content of 2% of steel fibers, which have a length of 13 mm (0.51 in), a diameter of 0.2 mm (0.0078 in), a yielding stress of about 2860 MPa (414 kpsi) and a Young's modulus of 200 GPa (29007 kpsi). The UHPFRC mechanical properties after heat treatment (24 hours at 90°C and 100% RH) were characterized at 28 days and the mean values were as follows: Young's modulus in compression 58.2 GPa (8441 kpsi) and compressive strength 198.2 MPa (28.7 kpsi). The flexural behavior was also characterized by means of a 4 Point Bending Test (4PBT) on thin beams with dimensions of 420 mm (16.5 in) × 110 mm (4.3 in) × 30 mm (1.2 in) (span × width × height) according to the AFGC recommendations (AFGC, 2013). The moment vs. deflection relationships are plotted in Figure 1.a.



(a)　　　　(b)
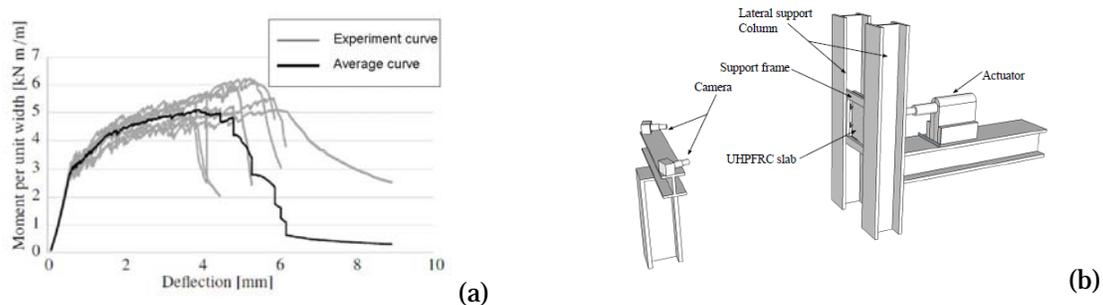
**Figure 1. Moment vs. deflection curves measured on the bending test of thin beams (1 mm=0.039 in; 1 kN m/m = 0.224 kip ft/ft).**

Square slabs with a thickness of about 30 mm (1.18 in) and width of about 500 mm (19.68 in) side were cast according to two different configurations (Figure 2.a): (i) a slab without casting defect for which fresh concrete was poured from a corner, letting the flow fill the whole

casing (Figure 2.b) ; (ii) a slab with a casting defect for which the fresh UHPFRC was poured from two opposite corners of the slab casing, while a thin plate of aluminum was used as a divider to stop the concrete flow from both parts of the casting (Figure 2.c). Once the fresh concrete had filled the mould, the aluminum divider was removed. This defect caused a discontinuity in the fiber distribution along a plane and it can represent a cold joint, which can occur in real-field casting process. The defect line was placed at 2/3 of the slab side, which means at about 166 mm (6.53 in) from the loading axis. Different colorants (brown and grey) were added to distinguish the concrete cast from the two casting corners. The marked line in Figure 2c indicates the defect.



(a)           (b)           (c)
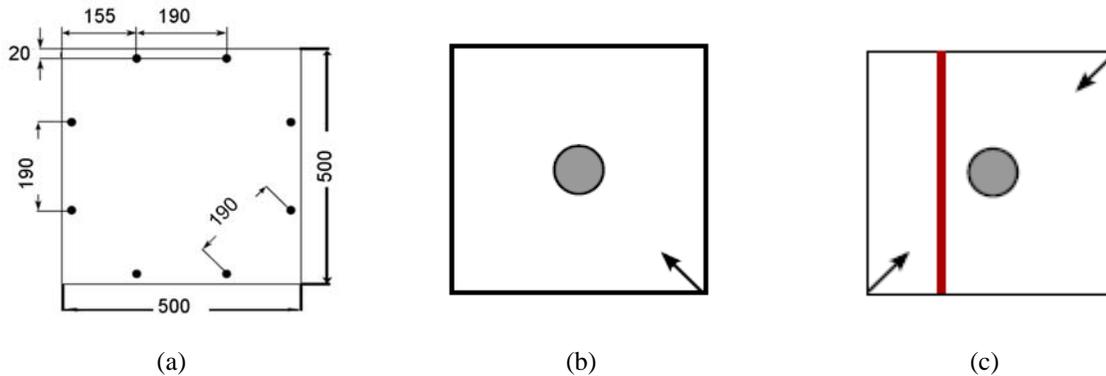
**Figure 2. (a) Geometry of the UHPFRC slabs (units in mm; 1 mm=0.039 in); (b) slab without defect; (c) slab with casting defect (arrow= casting direction, the grey circle = load).**

### 2.2. Punching 2-way slab test set-up

In order to ease the Digital Image Correlation (DIC) analysis, the slabs were tested in vertical position with a horizontal load (Figure 1.b). A steel frame was used to support the slab on the testing machine. The slab was supported by 8 flange-mounted balls located along a circle with a diameter of about 500 mm (19.68 in) as shown in Figure 2.a. Each support steel-sphere had a diameter of about 38 mm (1.50 in) and a maximum load bearing capacity of about 10 kN (2.248 kip). To prevent local crushing at the support locations, a 3.5 mm (0.14 in) thick steel plate was glued under each sphere as load diffuser. Moreover, each sphere was placed in a larger convex support which allowed their movement so that the horizontal reaction is negligible. Two digital cameras were placed at a distance of 2.1 m (82.7 in) and at an angle of 16°. The horizontal actuator load was controlled in a closed-loop by imposing a constant displacement at a speed of 1 mm/min for slab without defect and of 0.5 mm/min (0.02 in/min) for slab presenting defects in order to maintain a reasonable amount of data collected during the testing. The loading rate was accelerated to 1 mm/min (0.04 in/min) after 14 minutes of loading, when the full crack pattern had clearly developed. The head of the actuator was designed for a test as prescribed in the ASTM norm C1550-10a labs. The round head had a radius of about 50 mm (1.97 in) and a curvature radius of about 80 mm (3.15 in).

### 2.3. Digital image correlation

The surface of the slab was painted in two steps: first a white coating was applied in the center of the surface of the slab; then small dots of size 0.5-2 mm (0.02-0.079 in) were sprayed randomly on the white surface of the slab with black paint. For all tests, the area of the slab which was visible to DIC analysis was about $300 \times 300$ mm (11.81 in × 1.81 in) on the center of

the slab. As for DIC analysis, the image resolution was optimized with respect to the shooting rate. The two employed Nikon D7100 digital cameras had an effective resolution of $6000 \times 4000$ pixels. Pictures were captured at a constant interval of 15 seconds for all tests and both pictures were taken simultaneously via wired computer control. Both cameras were bolted directly into a rigid steel frame and the objective of the camera was supported by a polymer plate on a rigid steel frame.  In order to perform stereo-vision DIC analysis, the calibration of the stereovision system first needs to be performed (Sutton et al., 2009). Once the displacement is obtained, the 3D surface and displacement fields are reconstructed using a global finite element formulation (Besnard et al., 2006). Regular meshes of quadrangular elements are defined on the initial image of the sample surface from the left camera. From the displacement field, strains are estimated using the finite element shape functions of the element mesh, which are standard bilinear first order.

### 2.4. Magnetic-Inductance Method (MIM) to measure fiber orientation

Because of the ferromagnetic behavior of steel fibers, a UHPFRC may be regarded as consisting of two phases with strongly different magnetic permeability: the cement-based matrix and the fibers. Owing to the generally quite low volume fraction of the steel fibers, the interactions between them can be neglected and the effective permeability of the composite depends on the permeability of the matrix and of the fibers, on the fiber volume fraction and on their aspect ratio. The measurement of a magnetic-inductance parameter can hence be used to assess both the local average concentration and preferential orientation of fibers (Ferrara et al., 2012). This method has been implemented by means of the experimental set-up shown in Fig. 3: it consists of a C-shaped N87 ferrite core with a 78-turn coil wound around it, which is charged with a 100 mA sinusoidal current, providing the magnetic flux. When the magnetic core is leant against the UHPFRC specimen, the magnetic flux flows also through the specimen and the impedance measured at the terminals of the equivalent electrical circuit can be expressed from Eq.(1) as follows:

$$Z = R_c + j\omega[L_1 + L_V] \quad (1); \qquad\qquad f_\alpha = \frac{\Delta L_\alpha}{0.25\left(\Delta L_0 + \Delta L_{45} + \Delta L_{90} + \Delta L_{135}\right)} \quad (2)$$

where $R_c$ denotes the resistance of the coil and $L_l$ and $L_v$ respectively denote the magnetic inductance of the magnetic flux outside and through the specimen. The inductance $L_v$ can be split into a matrix contribution $L_{v0}$ and an incremental contribution $\Delta L_{v,fibers}$, which depends on the fiber volume fraction and orientation. Whereas inductance $L_v$ depends on the measurement frequency, compensated inductances result independent (Ferrara et al., 2012). The latter is defined as the difference between the inductance of the fiber reinforced composite and the inductance of the plain matrix, which coincides with that measured in free air.

The UHPFRC slabs were analyzed according to different "cell-schemes" as shown in Figure 3 (arrows indicating the direction of casting), measurements in each cell being taken along four different directions, namely at 0°, 45°, 90° and 135° to a reference y-axis. For each direction measurements were repeated four times, and reference will be made henceforth to the average of the four values. Quantitative assessment of the local concentration of fibers for each of the measured slab cells was performed through the calibration of the relationship between the "nominal average compensated inductance" and the nominal fiber content in the mix. The former is defined as the average, computed over the whole slab, of the averages of the compensated inductance as measured along the four directions for each cell. By means of such calibration, the

average values of compensated inductance for each cell could be processed to assess whether and to what extent the local concentration of fibers differed from the assumed nominal value. For the assessment of fiber orientation, "fractional" compensated inductances along each considered direction were calculated from Eq. (2), where α is the angle for each of the separately considered measurement directions. The fractional compensated inductance hence quantifies how much the inductance measured along one particular direction differs from the perfect isotropy value.



| (a) | (b) | (c) | (d) |
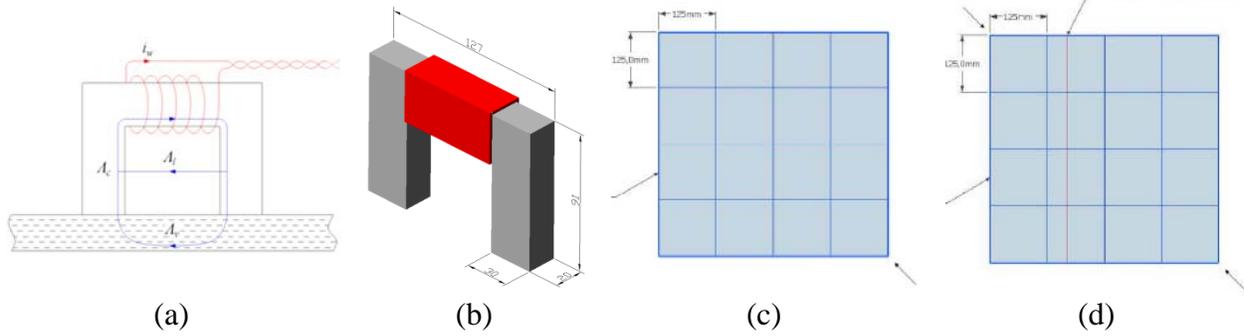
**Figure 3. (a) Scheme of the measurement set-up; (b) employed magnetic probe; schematic cell definition for cell slab without defect (c) and with defect (d).**

## 3. Results

### *3.1. Fiber Orientation*

In Figure 4 the direction of the measured maximum compensated inductance has been plotted, and compared to casting flow lines. The proposed procedure which compares the average of the four cell measurements to the average of the averages over the whole slab, has allowed discriminating the local fiber concentration. The color range in Figures 4 (c) and (d) from blue to yellow indicates an increase of the local concentration of fibers. Differences in local fiber concentration are evident and are the result of some dynamic segregation of fibers along the casting flow (Figure 4.a) or because some fiber segregation occurred in the bucket employed to cast the two different parts of the slab separated by the discontinuity (Figure 4.b). Interestingly the plotted fiber concentration-orientation graphs can be compared to the crack pattern of Figure 6 as detected during the mechanical tests by DIC analysis.



| (a) | (b) | (c) | (d) |
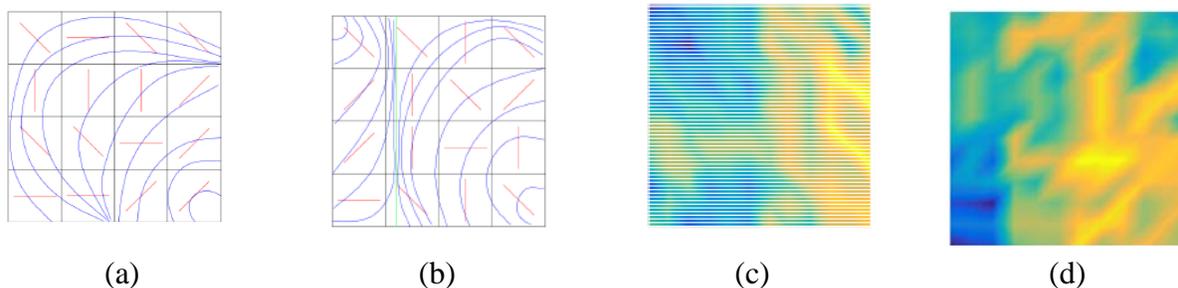
**Figure 4: Direction of maximum compensated inductance and inferred casting flow lines: (a) slab without defect; (b) slab with third side defect. Plots of fractional compensated inductances weighed by local fiber concentration: (c) slab without defect; (d) slab with third side defect.**

The correspondence between the two patterns is fairly remarkable: since the preferred orientation of the fibers clearly results in a strong anisotropy, one can note that the direction

orthogonal to the preferential fiber alignment offers a weaker post-cracking resistance. As cracks are expected to form at a right angle to the direction of weakest tensile resistance, the coincidence between crack path and direction of preferential fiber alignment is visibly explained.

### 3.2. Mechanical results with image analysis

Figure 5.a and 5.b show the load vs. deflection curves for all slabs tested in configuration without and with defect, respectively. All the slabs exhibited a flexural mode of failure without any conical crack surface due to shear punching. The test repeatability was excellent for both slab configurations. Table 1 summarizes the load and displacement values at the end of linearity and the peak load for both slabs. On average, the defect reduces the maximum load ($P_{max}$) of about 6% and the corresponding displacement ($\delta_{max}$) of about 20 %, as compared to the slabs without any casting defect.

Figure 6 shows the crack patterns during the punching test and the displacement field at the end of test for reference slabs of both configurations. Figures 6.a and 6.b show the microcrack pattern at a deflection of 7 mm (0.27 in) (before peak load), 10 mm (0.39 in) (at the peak load), and 13 mm (0.51 in) (after crack localization in yield lines), for the slab without and with defect, respectively. The crack pattern at the peak load (deflection of about 10 mm; 0.39 in) is rather complex for both configurations and does not correspond to the fully developed yield lines which are visible at the end of tests. For both configurations, micro-cracks showed a diffused pattern before the peak load. However, the defect line changed the microcracks from a radial pattern to parallel lines. Figure 6.c and 6.d show the displacement field and the yield lines at the end of the test which have a cross shape for the slab without defect (Figure 6.c) and a complex 3 line shape for the slab with defect (Figure 6.d).
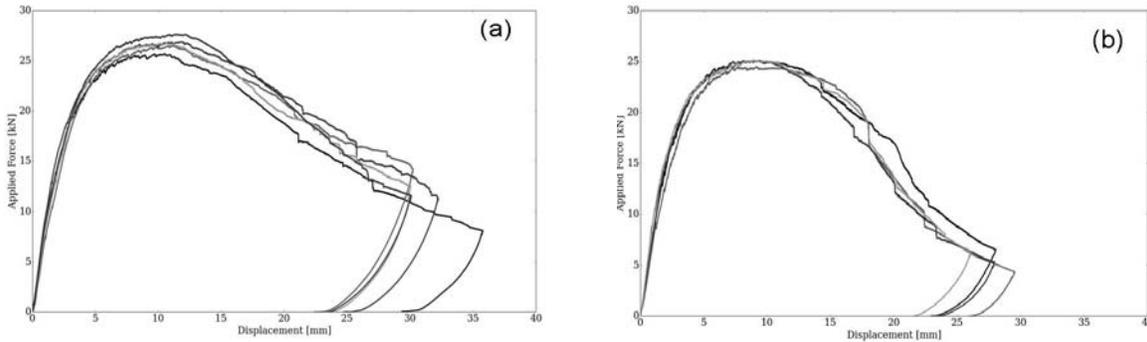


**Figure 5. Load vs. displacement curves for the slabs without defect (a) and the slabs with defect (b).**

Table 1. Load and displacement at the end of elasticity and maximum load ($P_{cr}$ and $\delta_{cr}$ are the load and displacement at the end of linearity, $P_{max}$ and $\delta_{max}$ are the load and displacement at the peak load)

|  | Pcr [kN] (kip) | δcr [mm] (in) | Pmax [kN] (kip) | δmax [mm] (in) |
|---|---|---|---|---|
| Slab w/o defect | 6.2 (1.39) | 0.9 (0.035) | 26.8 (6.02) | 10.1 (0.397) |
| Slab w/ one third defect | 7.8 (1.75) | 1.0 (0.039) | 25.1 (5.64) | 8.1 (0.319) |
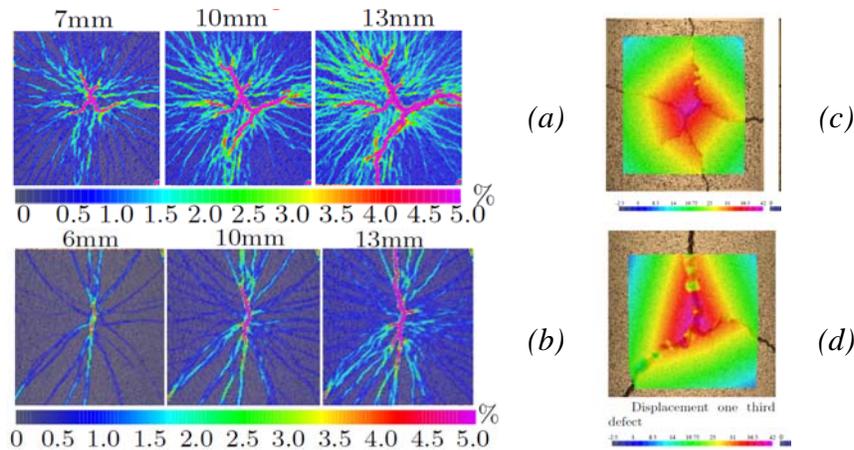
**Figure 6. Crack patterns at different displacement levels for slab without defect (a) and with defect (b). Deflection field at the end of testing: slabs without defect (c) and with defect (d).**

## 4. Conclusions

This work investigates the cracking behavior of some thin UHPFRC slabs with defects on the fiber distribution by means of DIC analysis and MIM technique (Baril, 2016). Based on the present results the following preliminary conclusions can be drawn:

(i) For the tested configuration of the UHPFRC slabs under punching loading, the presence of a prearranged defect of the casting flow affected more the ultimate deformation (- 20 %) than the flexural strength (- 6 %);

(ii) DIC analysis showed that the defect line affected the microcrack orientation and the crack pattern at the peak load;

(iii) MIM showed that the orientation of fibers was affected by the casting flow barriers and that the fibers mean direction well explains the change of crack pattern from radial to parallel microcracks.

## 5. References

Aubry, S., Bompas, P., Vaudeville, B., Corvez, D., Lagrange, T., Mazzacane, P., Brizou, A., 2015. A UHPFRC cladding challenge: the fondation Louis Vuitton pour la création « Iceberg ». RILEM-fib-AFGC International Symposium on Ultra-High Performance Fibre-Reinforced Concrete, 37-48.

Baril, M. Effet de défauts de coulage sur la micro-fissuration des dalles minces en béton fibré aux ultrahautes performances par stéréovision et corrélation d'images digitales, Master Thesis, Université Laval, Avril 2016.

Besnard, G., Hild, F., Roux, S., 2006. "Finite-element" displacement fields analysis from digital images: application to Portevin–Le Châtelier bands. Exp. Mech. 46, 789–803.

Association Française de Génie Civil (AFGC), 2013. Bétons fibrés à ultra-hautes performances – Recommandations, Paris.

Brühwiler, E., Denarié, E., 2008. Rehabilitation of concrete structures using ultra-high performance fibre reinforced concrete. UHPC-2008: The Second International Symposium on Ultra High Performance Concrete, March 05-07, Kassel, Germany, 895-902.

Ferrara, L., Faifer, M., Toscani, S., 2012. A magnetic method for non destructive monitoring of fiber dispersion and orientation in steel fiber reinforced cementitious composites—part 1: method calibration. Mater. Struct. 45, 575–589.

Marchand, P., Baby, F., Al Khayer, W., Attrach, M., Toutlemonde, F., 2012a. Modelling Flexural Tests on UHPFRC Thin-Walled Structures. Presented at the Hipermat, 757-764.

Marchand, P., Gomes, F., Dieng, L., Baby, F., Renaud, J., Massotte, C., Estivin, M., Billo, J., Bazin, C., Lapeyrere, R., Siegert, D., Toutlemonde, F., 2012b. Behaviour of an Orthotropic Bridge Deck with a UHPFRC Topping Layer. Siegert D., Toutlemonde F., Hipermat, 905-912.

Moreillon, L., Nseir, J., Suter, R., 2012. Shear and flexural strength of thin UHPC slabs. Hipermat Kassel 748–756.

Resplendino, J., 2004. First recommendations for ultra-high-performance concretes and examples of application. International Symposium on Ultra High Performance Concrete, Kassel, 79–90.

Russell, H.G., Graybeal, B.A., 2013. Ultra-High Performance Concrete: a state-of-the-art Report for the Bridge Community, PUBLICATION FHWA-HRT-13-060, June 2013.

Schmidt, M., Fehling, E., 2005. Ultra-high-performance concrete: research, development and application in Europe. ACI Spec. Publ. 228, 51–78.

Sutton, M.A., Orteu, J.J., Schreier, H., 2009. Image correlation for shape, motion and deformation measurements: basic concepts, theory and applications. Springer Science & Business Media.

Ter Maten, R.N., Grünewald, S., Walraven, J.C., 2013. UHPFRC in large span shell structures. Proceedings of the RILEM-fib-AFGC international symposium on ultra-high performance fibre-reinforced concrete, RILEM PRO 87, 1-3 October, Marseille, France, 327-334.

Toutlemonde, F., Resplendino, J., Sorelli, L., Bouteille, S., Brisard, S., 2005. Innovative design of ultra high-performance fiber reinforced concrete ribbed slab: experimental validation and preliminary detailed analyses. Spec. Publ. ACI 228, 1187–1206.

Toutlemonde, F., Resplendino, J., 2013. UHPFRC 2013 RILEM Pro 87.

Toutlemonde, F., Resplendino, J., 2011. Designing and Building with UHPFRC. Eds: Toutlemonde & Resplendino, John Wiley & Sons.

## 6. Acknowledgements